

High-Quality CEST Mapping with Lorentzian-model Informed Neural Representation

Chu Chen, Yang Liu, Se Weon Park, Jizhou Li, *Senior Member, IEEE*, Kannie W. Y. Chan, Jianpan Huang, Jean-Michel Morel, Raymond H. Chan,

Abstract—Chemical Exchange Saturation Transfer (CEST) MRI has demonstrated its remarkable ability to enhance the detection of macromolecules and metabolites with low concentrations. While CEST mapping is essential for quantifying molecular information, conventional methods face critical limitations: model-based approaches are constrained by limited sensitivity and robustness depending heavily on parameter setups, while data-driven deep learning methods lack generalizability across heterogeneous datasets and acquisition protocols. To overcome these challenges, we propose a Lorentzian-model Informed Neural Representation (LINR) framework for high-quality CEST mapping. LINR employs a self-supervised neural architecture embedding the Lorentzian equation – the fundamental biophysical model of CEST signal evolution – to directly reconstruct high-sensitivity parameter maps from raw z-spectra, eliminating dependency on labeled training data. Convergence of the self-supervised training strategy is guaranteed theoretically, ensuring LINR’s mathematical validity. The superior performance of LINR in capturing CEST contrasts is revealed through comprehensive evaluations based on synthetic phantoms and in-vivo experiments (including tumor and Alzheimer’s disease models). The intuitive parameter-free design enables adaptive integration into

diverse CEST imaging workflows, positioning LINR as a versatile tool for non-invasive molecular diagnostics and pathophysiological discovery.

Index Terms—CEST MRI, CEST Mapping, Self-supervised Learning, Implicit Neural Representation

I. INTRODUCTION

CHEMICAL Exchange Saturation Transfer (CEST) imaging has emerged as a powerful MRI technique for non-invasive molecular imaging and quantitative mapping of endogenous metabolites and exogenous agents in biological tissues. By selectively saturating exchangeable protons on molecules of interest, such as proteins, peptides, or metabolites [2]–[4], CEST enables the indirect detection of their concentrations via the water signal. This method provides a sensitive approach to detecting subtle biochemical changes in tissues, which makes it particularly valuable for applications in oncology, neurology, and metabolic studies [5], [6].

CEST imaging has shown great potential for mapping biomolecules, including Amide Proton Transfer (APT) for detecting mobile proteins [7], nuclear Overhauser effect (NOE) for aliphatic protons of lipids [8], [9], and various metabolite-specific CEST contrasts for creatine [10], [11], glucose [12] and glutamate [13], [14]. These endogenous contrasts can serve as biomarkers for different pathologies, such as tumors [15], ischemia [16], and Alzheimer’s disease (AD) [17]–[19].

A key step in CEST imaging is performing CEST analysis (mapping) on the source image data to identify the distribution and intensity of the molecules (pools) of interest. The general process is outlined in Fig. 1. Despite its promise, CEST mapping remains technically challenging due to several factors. The signal strength of CEST contrast is often low, requiring high-field MRI and advanced post-processing techniques for reliable quantification. As a result, robust modeling and signal processing techniques are essential to extract meaningful information from CEST imaging experiments.

In recent years, CEST analysis studies have focused on improving the sensitivity and specificity of the technique [20]–[22]. Novel image reconstruction and analysis methods, such as deep learning models, have also been explored to enhance

A preliminary version of this work was presented at the 21st IEEE International Symposium on Biomedical Imaging (ISBI2024) [1].

This work is partially supported by HKRGC Grants No. CityU11301120, C1013-21GF, CityU11309922, CityU9380162, ITF Grant No. MHP/054/22, LU BGR 105824, and InnoHK-Hong Kong Centre for Cerebro-cardiovascular Health Engineering.

Chu Chen is with the Department of Mathematics, City University of Hong Kong, Hong Kong, and Hong Kong Centre for Cerebro-cardiovascular Health Engineering, Hong Kong. (chuchen4-c@my.cityu.edu.hk)

Yang Liu and Se Weon Park are with the Department of Biomedical Engineering, City University of Hong Kong, Hong Kong, and Hong Kong Centre for Cerebro-cardiovascular Health Engineering, Hong Kong.

Jizhou Li is with the Department of Electrical Engineering, The Chinese University of Hong Kong, Hong Kong.

Kannie W. Y. Chan is with the Department of Biomedical Engineering, City University of Hong Kong, Hong Kong, Hong Kong Centre for Cerebro-cardiovascular Health Engineering, Hong Kong, and Russell H. Morgan Department of Radiology and Radiological Science, Johns Hopkins University School of Medicine, Baltimore, MD, USA

Jianpan Huang is with the Department of Diagnostic Radiology, The University of Hong Kong, Hong Kong.

Jean-Michel Morel is with the Department of Mathematics, City University of Hong Kong, Hong Kong.

Raymond H. Chan is with the Department of Operations and Risk Management and School of Data Science, Lingnan University, Hong Kong, and Hong Kong Centre for Cerebro-cardiovascular Health Engineering, Hong Kong.

CEST quantification and increase the robustness of the measurements [18], [23]–[26]. These advancements aim to push the boundaries of CEST imaging from experimental settings to widespread clinical use, allowing for more precise and non-invasive molecular diagnostics.

In this context, we propose an algorithm to improve the accuracy and efficiency of CEST analysis by leveraging neural network-based representations informed by the Lorentzian model. By combining deep learning with domain-specific knowledge, this approach seeks to overcome the limitations of current CEST quantification methods, offering improved sensitivity and resolution of CEST contrast. The contributions of this work can be summarized as:

1) *Novel framework for CEST mapping*: We propose a novel framework, Lorentzian-model Informed Neural Representation (LINR), that improves the extraction of high-quality CEST contrast by fully leveraging multi-layer perceptrons (MLPs) of implicit representation to continuously distributed parameters. Additionally, LINR requires no expert knowledge of CEST imaging or ground truth molecular contrast for reference, making it accessible and user-friendly for researchers without specialized training and external datasets.

2) *Theoretical analysis*: We mathematically prove the convergence of our neural network in approximating CEST data by constructing a Lorentzian Neural Tangent Kernel (LNTK), ensuring the stability and reliability of the model, along with linear convergence speed for the mapping process.

3) *Superior performance on both synthetic phantoms and in vivo data*: We introduce a Lorentzian-model-based simulation method that models noisy phantoms with spatial variance, providing a fully invertible evaluation. Extensive experiments on synthetic phantom data demonstrate the superior performance of our method in comparison to traditional approaches, showing its robustness across various noise levels. The proposed approach has also been successfully applied to in vivo datasets from tumor and Alzheimer’s disease cases. It shows compatibility with pathological observations and outperforms carefully tuned conventional fitting methods.

II. RELATED WORK

A. Denoising

CEST imaging is highly sensitive to small changes in molecular composition, but its precision can be compromised by noise arising from various sources, such as scanner imperfections and low signal-to-noise ratio (SNR). This noise can obscure subtle contrast differences, leading to inaccurate quantification of CEST effects. Several denoising methods have been proposed to enhance the accuracy of CEST contrast measurements, such as MLSVD [27], NLmCED [28], DECENT [29], DCAE-CEST [30], and IRIS [1]. Notably, the DCAE-CEST employs an encoder-decoder network trained on simulated z-spectra with Kullback-Leibler divergence constraints, and validated via adaptive learning using principal component analysis. While the IRIS leverages the ability of neural networks to continuously represent subspace structures and its excellent implicit regularization, demonstrating outstanding performance in CEST denoising compared to

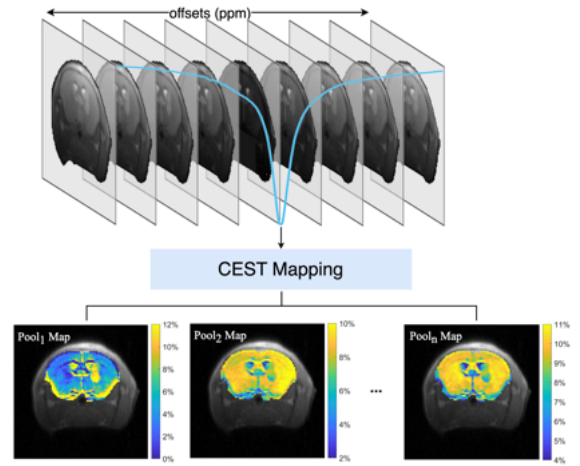


Fig. 1. Illustration of the CEST analysis process, where the CEST contrast of each exchangeable pool is obtained by mapping from the CEST image sequence, which is shown on top. The blue curve indicates the usual contrast change of CEST images.

other methods and eliminating the supervised training phase, including that on simulated data. Therefore, we integrated IRIS as a denoising module into our framework to improve the precision of CEST imaging.

B. CEST Mapping

CEST mapping is an analysis process that extracts CEST contrast from the given CEST sequence (z-spectra). Generally, z-spectrum analysis involves quantifying CEST contrast by calculating the difference between the acquired z-spectrum (z) and a reference spectrum (z_{ref}). The most commonly used CEST effect extraction model is the Lorentzian-line-fit analysis [31] due to its ability to model the shape of the z-spectrum, particularly the saturation transfer effects of exchanging protons. The Lorentzian line shape can account for multiple exchange pools (e.g., amide, amine, hydroxyl) by the Multi-pool Lorentzian Fitting (MPF). In MPF, CEST effects are parameterized by the Lorentzian model and can be estimated by solving a non-linear least squares fitting problem,

$$\hat{p} = \arg\min_p \frac{1}{2} \|L(p, \Delta\omega) - z\|_2^2, \quad (1)$$

where L is the Lorentzian model defined in Eq. (9), p represents the parameters related to exchangeable pools and $\Delta\omega$ is saturation frequency (offsets). Since MPF involves optimizing multiple parameters (such as amplitude, width, and center frequency for direct water saturation), the outcome of the fitting process can be highly sensitive to how it is initialized and constrained, where the complexity of fitting multiple overlapping Lorentzian peaks can make the fitting process more sensitive to these choices. A poor optimization setup may lead to local minima and bad convergence rates.

Due to the large number of parameters required for setting bound and initial values, it becomes impractical to fine-tune each one individually when dealing with a large number of CEST targets. As a result, alternative approaches are being sought. Magnetization Transfer Ratio Asymmetry (MTR_{asym}) analysis is one of the simplest and most widely

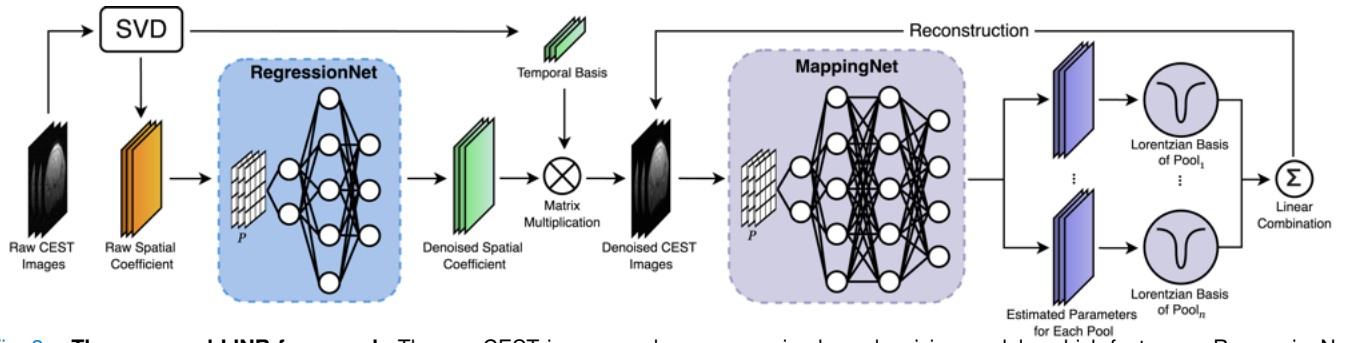


Fig. 2. The proposed LINR framework. The raw CEST images undergo processing by a denoising module, which features a RegressionNet. This network is optimized by regressing the noisy spatial coefficients obtained from truncated singular value decomposition (SVD). The denoised CEST sequence is then reconstructed by multiplying the denoised coefficients from the RegressionNet output with the temporal basis. Next, the denoised sequence is fed into the MappingNet, which estimates parameters that aid in reconstructing the CEST data using the Lorentzian model. The MappingNet is optimized by minimizing the loss between the reconstructed images and the denoised CEST images. Both networks take the coordinate grid P as input.

used methods for quantifying CEST contrasts. It measures the asymmetry of the z-spectrum by calculating the difference between signals at positive and negative frequency offsets relative to water resonance. The method is prone to errors from background effects, such as direct water saturation and magnetization transfer. Additionally, it fails to account for multiple exchanging pools, limiting its effectiveness in complex biological environments. Polynomial and Lorentzian Line-Shape Fitting (PLOF) [22] uses a polynomial function to model the background signals (z_{ref}) and Lorentzian line shapes to capture the chemical exchange effects. However, the fitting process in PLOF is still sensitive to the choice of initial guess and the bound setup. The Total Generalized Variation (TGV) [32] method is a powerful denoising technique that has been applied to CEST imaging to improve the accuracy of the analysis by enforcing smoothness in the CEST contrast. The downside of TGV is that it introduces regularization parameters that must be carefully tuned. If not balanced correctly, TGV can either oversmooth the data or fail to suppress enough noise, leading to a loss of important CEST contrast information. DeepCEST [18], [23] leverages neural networks to fit MPF estimation results during the training phase, enabling rapid predictions for new samples during testing. This approach eliminates the need for constraint settings for unknown individuals. However, during training, a large amount of CEST data must still undergo MPF prediction to create training pairs. Additionally, if the data acquisition settings (e.g., field strength and saturation frequency) differ, DeepCEST struggles to generalize to new data distributions, requiring retraining on newly collected data under the according settings [18].

In this article, we focus on Lorentzian parameter mapping, and without loss of precision, we still refer to this process as CEST mapping, similar to existing works [22], [27], [33], [34].

C. Implicit Neural Representation

Implicit Neural Representation (INR) is a powerful approach that is gaining attention in the field of computer vision. Instead of storing data in a traditional grid or pixel-wise

format, INRs learn a continuous mapping from spatial coordinates to data values using neural networks. This approach allows for efficient representation of complex signals, such as images [35], [36] or 3D shapes [37].

Liu *et al.* [38] proposed the INRESP algorithm to improve CEST image reconstruction. INR was first introduced for CEST acceleration and trained to represent the real and imaginary parts of CEST images without the need for extra fully sampled k-space data.

In LINR, we fully unleash the power of INRs in subspace modeling and represent the parameter space of the Lorentzian model, enabling a self-supervised algorithm for high-sensitivity CEST imaging that eliminates the external training phase and requires no noise-free data or ground truth Lorentzian parameter for network optimization.

III. METHOD

A. Denoising

We denote a coordinate grid of size $M \times N \times 2$ by $P = \{x\}_{M \times N}$, where each $x \in \mathbb{R}^2$ is a coordinate point encoding horizontal and vertical indices. With the additive noise assumption for CEST data in $M \times N$ spatial dimensions and number of C offsets, the data formation model can be expressed as

$$\mathbf{y} = \mathbf{x} + \mathbf{n}, \quad (2)$$

where $\mathbf{x}, \mathbf{y} \in \mathbb{R}^{MN \times C}$ are vectorized matrices of underlying noise-free images and their noisy observation, respectively, while $\mathbf{n} \in \mathbb{R}^{MN \times C}$ is the noise matrix.

Adopting the concept of transformation-based denoising methods [39], [40], we can remove the noise-related coefficients \mathbf{u} of \mathbf{x} on an orthogonal basis \mathbf{v} obtained by singular value decomposition (SVD). Therefore, the denoising problem expressed in Eq. (2) can now be reformulated as an optimization problem

$$\arg\min_{\mathbf{u}} \frac{1}{2} \|\mathbf{u}\mathbf{v} - \tilde{\mathbf{u}}\mathbf{v}\|^2, \quad (3)$$

with suitable constraints on \mathbf{u} , where $\tilde{\mathbf{u}}$ represents the spatial coefficients of \mathbf{y} on the basis \mathbf{v} . Since \mathbf{v} is an orthogonal

matrix, Eq. (3) is equivalent to

$$\operatorname{argmin}_{\mathbf{u}} \frac{1}{2} \|\mathbf{u} - \tilde{\mathbf{u}}\|^2. \quad (4)$$

By keeping the first K principal components, we obtain the first regularized solution to Eq. (4), which can be rewritten in vectorized form as

$$\hat{\mathbf{u}} = D^K(\tilde{\mathbf{u}}). \quad (5)$$

where D^K is the projection operator on the first K principal components.

We now address the problem of defining suitable model constraints on $\hat{\mathbf{u}}$ to further denoise its components. Knowing the fact that outliers in the given data are overlooked when it is fitted by a smooth continuous function (*i.e.* regression), a denoising result can be obtained by taking the regression curve [1], [40]. Therefore, once K has been determined, our denoising algorithm involves a neural network called RegressionNet N_R to represent a continuous mapping $N_R(\cdot, \theta_R) : \mathbb{R}^{M \times N \times 2} \rightarrow \mathbb{R}^{M \times N \times K}$ with parameters θ_R . This network takes the coordinate grid P points as input and is optimized by solving

$$\hat{\theta}_R = \operatorname{argmin}_{\theta_R} \frac{1}{2} \|N_R(P, \theta_R) - \hat{\mathbf{u}}\|_2^2, \quad (6)$$

where the above minimization is performed simultaneously over all grid points and all channels by backpropagation and amounts to minimizing the loss function

$$\mathcal{L}_R = \frac{1}{2} \|N_R(P, \theta_R) - \hat{\mathbf{u}}\|_2^2. \quad (7)$$

An ℓ_2 -norm is applied here to prevent over-fitting after regression. Once the optimization is finished, the final denoised CEST data can be reconstructed as

$$\hat{\mathbf{x}} = N_R(P, \hat{\theta}_R) \mathbf{v}. \quad (8)$$

B. Mapping

The denoised CEST data is denoted by $Z \in \mathbb{R}^{M \times N \times C}$ and $z \in \mathbb{R}^C$ represents a given z-spectrum. The n -pool Lorentzian model $L : \mathbb{R}^{2n+2} \times \mathbb{R}^C \rightarrow \mathbb{R}^C$ mapping from molecules-related parameters to z-spectrum is defined by

$$L(p, \Delta\omega) = c - \frac{A_{DS}}{1 + (\frac{\Delta\omega - \delta_{DS}}{\Gamma_{DS}/2})^2} - \sum_{i \in \text{pools}} \frac{A_i}{1 + (\frac{\Delta\omega - \delta_{DS} - \delta_i}{\Gamma_i/2})^2}, \quad (9)$$

where direct saturation (DS) represents the water pool, and pools is the set of indices of the target molecular pools that are exchanged with water. For an n -pool Lorentzian model, each pool is parameterized by its amplitude A_i and peak width Γ_i , as well as the center frequency for direct saturation δ_{DS} and constant term c . Both 4-pool and 5-pool Lorentzian models are used in this study. A common 4-pool Lorentzian model includes the amide proton transfer (APT $\delta_{APT} = 3.5\text{ppm}$), relayed nuclear Overhauser effects (NOE $\delta_{NOE} = -3.5\text{ppm}$), and magnetization transfer (MT $\delta_{MT} = -2.5\text{ppm}$). The 5-pool Lorentzian model extends this by incorporating an additional guanidine (GuanCEST $\delta_{Guan} = 2\text{ppm}$) pool, reflecting origins from both creatine and arginine guanidine groups [33], [41], [42]. The CEST contrasts are generated by solving the

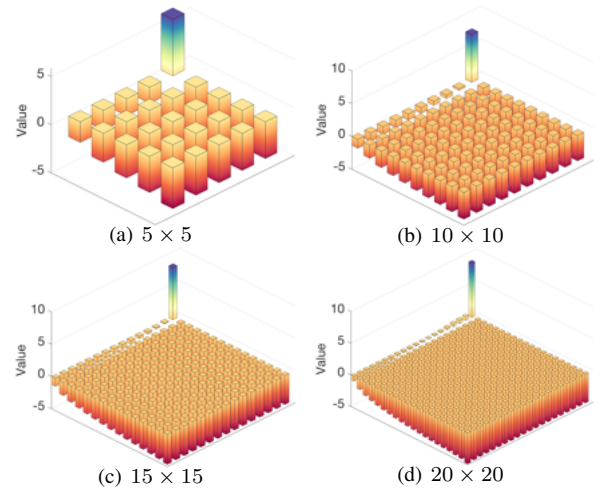


Fig. 3. Log of NTK eigenvalues with respect to different resolutions, which are indicated below each subfigure. The logarithm is applied for a better display range.

Lorentzian fitting problem and taking the optimal amplitude A_i maps. These spatially resolved contrasts provide molecular-level differentiation, which are related but not equivalent to the absolute concentration or exchange rate maps.

Since molecule-related parameters possess spatial variances, there is an underlying group of parameters p_x at a given location x . In LINR, p_x is estimated by a neural network called MappingNet as

$$p_x = N_M(x, \theta_M),$$

where θ_M is the trainable set of parameters of the network, and the network takes the z -spectrum that queries from a given location x as input.

The loss function \mathcal{L}_M is defined by

$$\begin{aligned} \mathcal{L}_M &= \sum_{x \in P} \|L(p_x, \Delta\omega) - z_x\|_1 \\ &= \sum_{x \in P} \|L(N_M(x, \theta_M), \Delta\omega) - z_x\|_1, \end{aligned}$$

where z_x is the denoised z-spectrum located at x . We opted for the ℓ_1 -loss instead of the traditional ℓ_2 regression to avoid overfitting outlier data points and z-spectra outside the region of interest (ROI).

The overall framework of the LINR algorithm is displayed in Fig. 2

C. Convergence Analysis

In the LINR algorithm, MappingNet performs regression within the parameter space of the Lorentzian model and is trained using Lorentzian-model-based self-supervised optimization through ℓ_1 -loss. In this section, we investigate the algorithm's convergence when applied to a given CEST data. For simplicity in derivations, we will abbreviate $L(p, \Delta\omega)$ as $L(p)$ and the weight θ_M of the MappingNet as θ in this section.

Assuming MappingNet is of depth d , with a Lipschitz, twice differentiable, bounded second derivative nonlinearity function

σ , and layers with width n_1, \dots, n_{d-1} . Examine the dynamics of weights in $N_M(x, \theta)$ updated by gradient descent,

$$\theta(t + \eta) = \theta(t) - \eta \nabla_{\theta} \mathcal{L}_M(\theta), \quad (10)$$

where η is the learning rate used during training, t is training time, and the loss $\mathcal{L}_M(\theta)$ is viewed as a function of θ . Therefore, as the learning rate converges to zero, the dynamics of weights follows

$$\frac{\partial \theta}{\partial t} = \lim_{\eta \rightarrow 0} \frac{\theta(t + \eta) - \theta(t)}{\eta} = -\nabla_{\theta} \mathcal{L}_M(\theta), \quad (11)$$

with

$$\nabla_{\theta} \mathcal{L}_M(\theta) = \nabla_{\theta} L(N_M(x, \theta)) \text{sign}(L(N_M(x, \theta)) - z_x). \quad (12)$$

Let $u(t, x) = L(N_M(x, \theta)) - z_x$ be the difference between the given z-spectrum and the one reconstructed from the estimated parameters. Then the dynamics of $u(t, x)$ follows

$$\begin{aligned} \partial_t u(t, x) &= \partial_t L(N_M(x, \theta)) \\ &= \nabla_{\theta} L(N_M(x, \theta))^T \partial_t \theta \\ &= -\nabla_{\theta} L(N_M(x, \theta))^T \nabla_{\theta} \mathcal{L}_M \\ &= -\sum_{x' \in P} K_L(x, x') \frac{\partial \mathcal{L}_M}{\partial L(p_{x'})} \\ &= -\sum_{x' \in P} K_L(x, x') \text{sign}(u(t, x')), \end{aligned} \quad (13)$$

where we define the Lorentzian Neural Tangent Kernel (LNTK) as

$$K_L(x, x') = \nabla_{\theta} L(N_M(x, \theta))^T \nabla_{\theta} L(N_M(x', \theta)). \quad (14)$$

By [43], the Neural Tangent Kernel (NTK) of the MappingNet $N_M(x, \theta)$ is

$$K(x, x') = \nabla_{\theta} N_M(x, \theta)^T \nabla_{\theta} N_M(x', \theta), \quad (15)$$

where x and x' are coordinates, $\nabla_{\theta} N_M(x, \theta)$ is the network's gradient with respect to θ . As the network weights are updated during training, the NTK also changes over time. However, as stated in *Theorem 1*, Jacot et al. [43] proposed that as the network becomes increasingly overparameterized, the NTK tends to converge towards a deterministic kernel which stays asymptotically constant during training.

Theorem 1 [43]: Assume a network is of depth d , with a Lipschitz, twice differentiable (second derivative bounded) nonlinearity function σ . Then in the limit as the layers' width $n_1, \dots, n_{d-1} \rightarrow \infty$, the NTK converges in probability to a deterministic limiting constant kernel:

$$K(x, x') \rightarrow K^{\infty}(x, x').$$

As the gradient of the Lorentzian model with respect to p is irrelevant to the network architecture or the given data, we have the following corollary for LNTK analogously,

Corollary: Assume a network is of depth d , with a Lipschitz, twice differentiable (second derivative bounded) nonlinearity function σ , in the limit as the layers' width $n_1, \dots, n_{d-1} \rightarrow \infty$. Then the LNTK converges in probability to a deterministic limiting constant kernel:

$$K_L(x, x') \rightarrow K_L^{\infty}(x, x'),$$

where $K_L^{\infty}(x, x') = \nabla_p L(p)^T K^{\infty}(x, x') \nabla_p L(p)$.

Furthermore, since MappingNet is both optimized and evaluated on the same CEST sequence, the limiting LNTK can be expressed on the coordinate grid by

$$K_L^{\infty}(P, P) = \nabla_p L(p)^T K^{\infty}(P, P) \nabla_p L(p), \quad (16)$$

where $P = \{x\}_{M \times N}$ represents all coordinates within the image domain.

Next, we will focus on the limiting kernel and explore the properties of the LNTK. Both the *Lemma* and *Theorem 2* demonstrate that the LNTK maintains the same positive definiteness as the NTK.

Lemma: Given any parameter vector $p \in \mathbb{R}^{2n+2}$ with no zero entry except for δ_{DS} , $\nabla_p L(p) \in \mathbb{R}^{(2n+2) \times C}$ is full rank.

Theorem 2: If limiting NTK $K^{\infty}(P, P)$ is strictly positive definite and the reduced parameter vector $p' \in \mathbb{R}^{2n+1}$ is with no zero entry, then the limiting Lorentzian Neural Tangent Kernel (LNTK) $K_L^{\infty}(P, P)$ is also strictly positive definite.

The assumption that the parameter vector has no zero entries is mild, as the network is optimized from random initialization. What's more, the underlying ideal parameter \tilde{p} will not have zero entry within the ROI except for δ_{DS} ($\delta_{DS} = 0$ will not affect the non-singularity of $\nabla_p L(p)$), such that the estimated output p during training still satisfies the assumption unless converged. For convenience, we denoted output parameter with δ_{DS} eliminated as $p' \in \mathbb{R}^{2n+1}$.

We continue to investigate the dynamics of $u(t, x)$ during training, which can be defined on all coordinates as $u(t, P) = L(N_M(P, \theta)) - Z$, and the dynamics can be expressed by the following equation,

$$\partial_t u(t, P) = -K_L^{\infty}(P, P) \text{sign}(u(t, P)), \quad (17)$$

The convergence of $u(t, P)$ is ensured by *Theorem 3*. The proofs of the mentioned lemma and theorems are given in the [Appendix A](#).

Theorem 3 (Convergence): If limiting NTK $K^{\infty}(P, P)$ is strictly positive definite and the parameter vector p' is with no zero entry, then

$$u(t, P) \rightarrow 0, \text{ as } t \rightarrow \infty,$$

and it is a linear convergence.

Therefore, the overparameterized MappingNet, relative to the CEST spatial resolution, ensures that the signal reconstructed through the Lorentzian model converges to the given z-spectrum. This also highlights the importance of the denoising module.

IV. EXPERIMENTS

We compared the effectiveness of different methods based on their experimental performance. By allowing both qualitative and quantitative evaluations, we assessed the analysis outcomes of MPF [31], PLOF [22], MPF with non-local means denoising (NLM), and LINR using synthetic phantoms. All experiments were conducted in Matlab (R2023a) or Python 3.8.17 on a PC equipped with Intel[®] Xeon[®] Silver 4210

Processor CPU 2.20GHz and Nvidia GeForce RTX 3090 GPU with 24G of memory.

To validate the applicability and advantages of our method for in vivo pathology, we tested it on a mouse brain tumor dataset and an AD dataset, comparing it against the widely used framework composed of MPF with MLSVD [27] pre-denoising. MPF’s initial/bound settings for different pathologies are detailed in [Appendix C](#).

LINR offers the benefit of not requiring initial/bound settings and using consistent hyperparameters across datasets. The RegressionNet is a position-encoding MLP with four hidden layers, while the MappingNet is of the same architecture but with six hidden layers; each layer contains 512 neurons with ReLU non-linearity. The truncation number K in the denoising module is set to 6. The MappingNet starts to train after the RegressionNet is fully optimized. During optimization, both the RegressionNet and MappingNet are trained with the Adam optimizer at a learning rate of 1×10^{-3} , for 20,000 and 10,000 epochs, respectively.

TABLE I
PARAMETER SETTINGS FOR EACH SYNTHETIC PHANTOM TYPE.

Phantom	Description	Parameter Range
A	Blank	$A_{APT} = A_{NOE} = 0\%$
B	Random+Blur	$A_{APT} = 0\%$ $A_{NOE} \in [10\%, 35\%]$
C	Random+Blur	$A_{APT} \in [10\%, 35\%]$ $A_{NOE} \in [10\%, 35\%]$
D	Gradient	$A_{APT} = 1.8Col - [18Col] \times 0.05^*$ $A_{NOE} = 1.8Row - [18Row] \times 0.05^*$

* Col and Row are indexes of columns and rows of the image, respectively.

A. Data Setup

We outline the data setup utilized, starting with synthetic phantoms, so that we can quantitatively evaluate the molecule mapping accuracy after inversion. The synthetic data is categorized into four distinct phantoms: A, B, C, and D, as visualized in Fig. [4\(a\)](#) GT phantom. Phantom A acts as a blank control group. For Phantoms B and C, parameters are randomly generated within a defined Lorentzian model parameter space and smoothed using Gaussian blurring to simulate spatial continuity, with the z-spectrum then simulated. Phantom D is a gradient phantom where parameters change linearly, with truncation at certain step sizes, across rows (columns) but remain constant within each column (row). The APT and NOE gradients are oriented perpendicularly, where quantification is detailed in [TABLE I](#). While each phantom incorporates variations in APT/NOE effects, all synthetic z-spectra include background effects (e.g., water and MT pools) with randomly sampled parameters and then smoothed with Gaussian kernels (see [Appendix B](#) for detailed setup).

Given that CEST contrast exhibits significant pathological features in mouse tumors and Alzheimer’s disease, we tested the effectiveness and rationale of LINR using in-vivo datasets of these two conditions. All animal experiments were approved by the Animal Ethics Sub-Committee and followed the institutional guidelines of the Institutional Laboratory Animal

Research Unit of the City University of Hong Kong, and were conducted under an authorized animal experiment license. All MRI experiments were performed on a horizontal bore 3T Bruker BioSpec system (Bruker, Ettlingen, Germany).

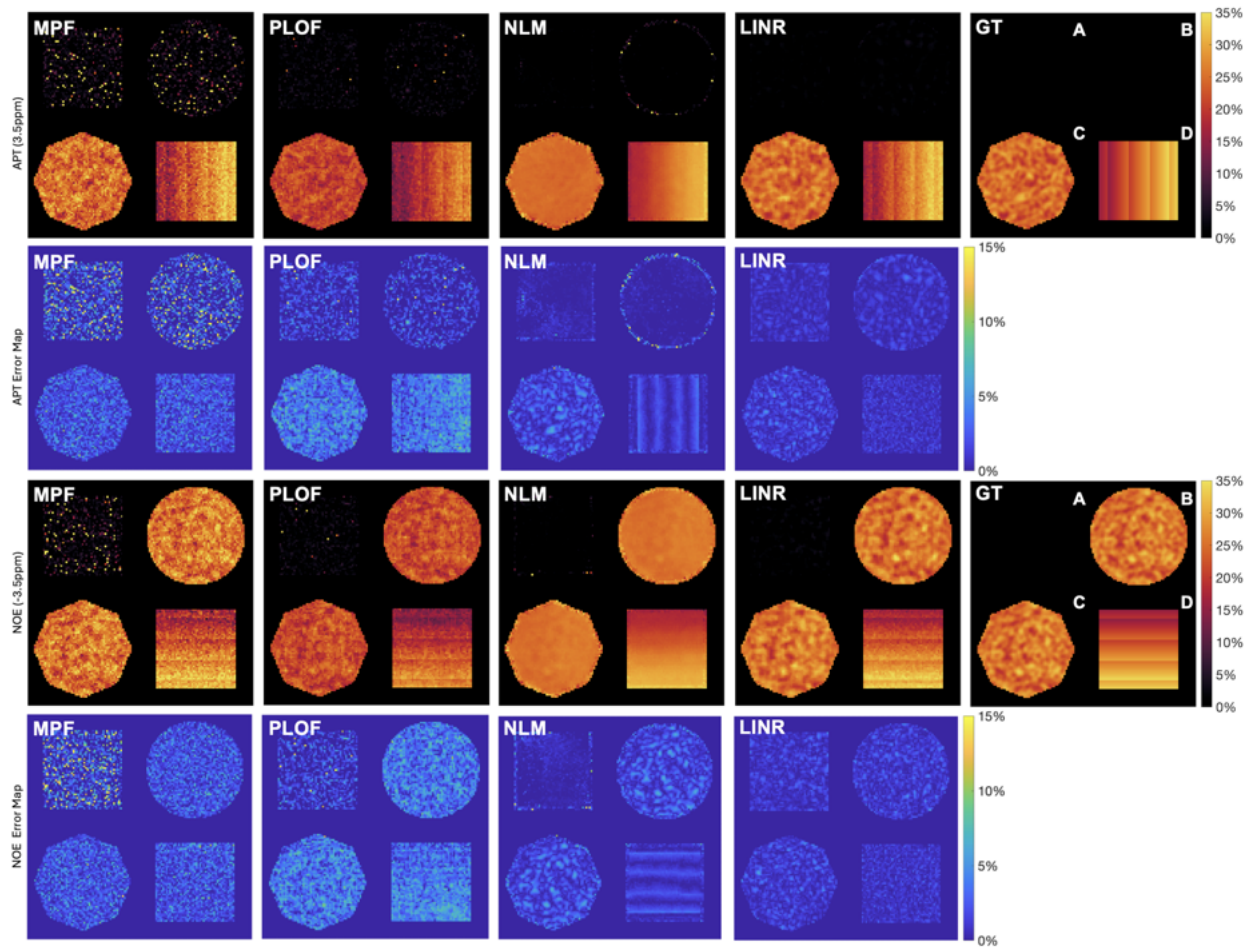
For in-vivo evaluation of tumor pathology, we prepared 10 sets of mouse data. Each of them was injected with U-87 MG cell ($0.5M/3ul$) at 2.0 mm right-lateral, 0.2 mm anterior, and 3.8 mm below the bregma [44]. The CEST MRI sequence was a continuous-wave (CW) saturation module followed by the rapid acquisition with refocused echoes (RARE) as a readout module. A power (B_1) of $0.8\mu T$ and a duration (t_{sat}) of 3000 ms were used for the saturation module. The saturation frequency varied from -15 to 15 ppm, with a 0.2 ppm increment between -7 and 7 ppm and a 2 ppm increment from -15 to -7 ppm and from 7 to 15 ppm. Four M_0 images with saturation frequency offset at 200 ppm were acquired and averaged for z-spectrum normalization. The readout parameters were as follows: repetition time (TR)=5000 ms, echo time (TE)=5.9 ms, matrix size=96×96 within a field of view (FOV) of 30×30 mm², slice thickness=1 mm, RARE factor=32.

For the dataset of AD, 15 AD mice (9 APP/PS1 and 6 5XFAD, 6 to 16 months, male, the Jackson Laboratory, Maine) and 10 age-matched (wild-type) WT mice (C57BL/6, male, the Jackson Laboratory, Maine) were used in this study. APP/PS1 mice are double transgenic mice expressing a chimeric mouse/human APP (Mo/HuAPP695swe) and a mutant human PS1 (PS1-dE9), both directed to neurons of the central nervous system. Both mutations are associated with early-onset AD. The CEST MRI sequence was also a CW saturation module, followed by RARE as a readout module. A saturation power (B_1) of $0.7\mu T$ and a duration (t_{sat}) of 2000 ms were applied in the saturation module. The saturation frequency ranged between -8 and 8 ppm, with increments of 0.2 ppm and 0.5 ppm increments from -8 to -5 ppm and from 5 to 8 ppm. Four M_0 images, with a saturation frequency offset at 200 ppm, were acquired and averaged for z-spectrum normalization. The readout parameters were repetition time (TR) of 4000 ms, echo time (TE) of 3.7 ms, matrix size 64×64 within a FOV of 20×20 mm², slice thickness of 2 mm, and RARE factor of 32.

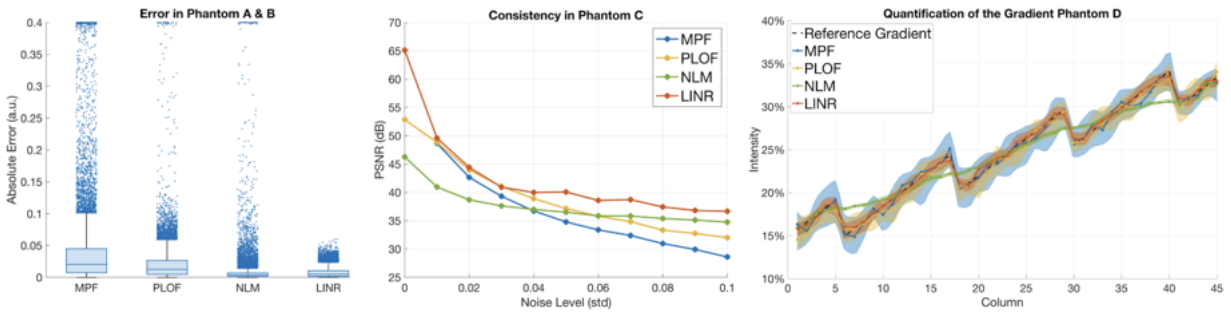
B. Synthetic Phantom

We applied the MPF [31], PLOF [22], and NLM, along with our LINR algorithm, to synthetic phantom data with additional Gaussian noise. Based on the visual comparison of the maps generated from the noisy synthetic phantoms in Fig. [4\(a\)](#), the LINR method stands out as the most effective technique in handling noise and preserving details across the entire range of synthetic phantoms, whose capacity to handle both the texture configurations of Phantoms B and C and the clean distribution in Phantom A underscores its robustness.

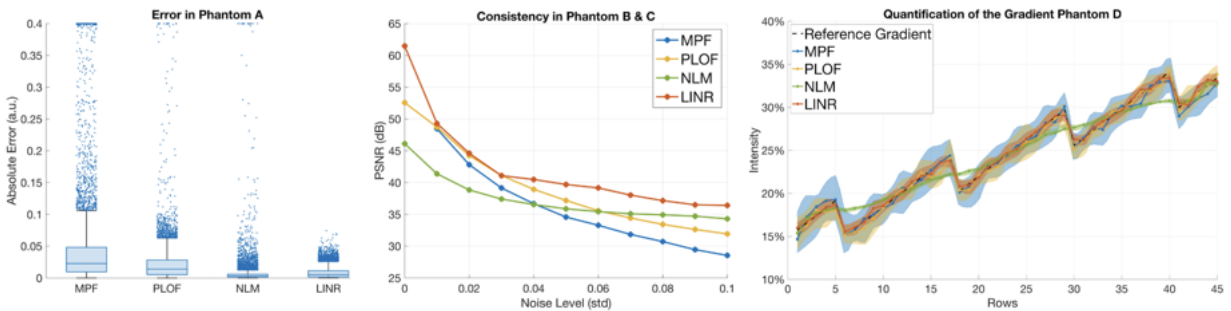
The boxplots on the left of Fig. [4\(b\)](#) and Fig. [4\(c\)](#) indicate the error distribution at the phantoms where the intensities should be blank. The performance of LINR is notably superior in maintaining the integrity of the gradient transitions in Phantom D, where linear parameter changes are clearly depicted with minimal distortion and truncations of the gradient are well detected.



(a) Visualization of maps generated from a synthetic phantom with 0.05 std of additive Gaussian noise.



(b) APT Maps Evaluation



(c) NOE Maps Evaluation

Fig. 4. Synthetic phantom evaluation. (a) CEST contrasts (3.5ppm upper and -3.5ppm lower) and the corresponding error maps generated by MPF, PLOF, NLM, and LINR on synthetic phantoms with 0.05 std of additive Gaussian noise. Ground truth maps are on the right. (b) and (c) are quantitative evaluations, where the boxplot (left) and band plot (right) are results from the same condition as (a).

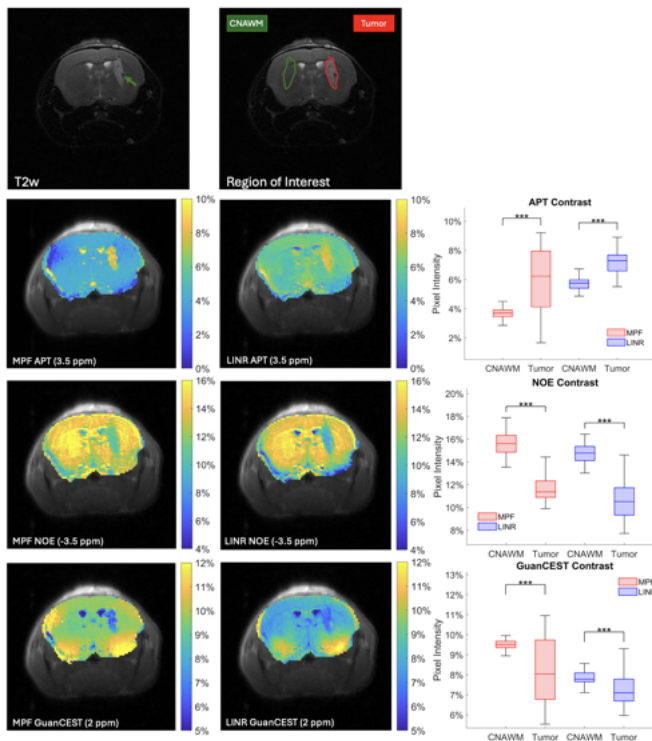


Fig. 5. CEST analysis on the mouse with brain tumor. Color CEST contrasts of the brain are overlaid on the averaged M0 image, where concentrated pools are specified at the bottom of each subfigure. The corresponding T2w image is on the top, and instructions on the ROIs are shown aside. In the T2w image, the arrow points to a group of low-brightness cells within the hyperintense area, which is a piece of normal tissue surrounded by the tumor. The boxplots on the right compare the intensity distribution of the CEST effect between the tumor region and its CNAWM. *** p -value < 0.001.

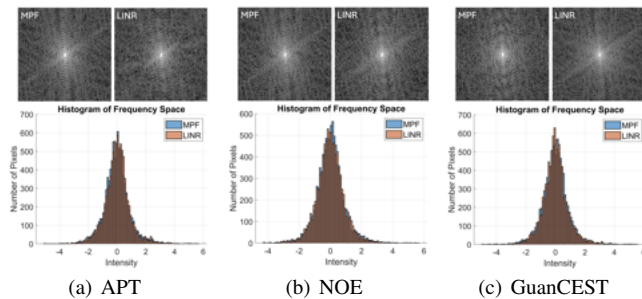


Fig. 6. Similarity evaluation of MPF and LINR in the frequency domain. The histogram of frequencies with respect to each contrast is plotted below the frequency space visualization, comparing the frequency distribution provided by the two methods. A logarithm is applied to the frequencies for a better display range.

To quantitatively assess the consistency of molecules with the same intensity under noise and the accuracy of gradient detection, the strip charts in Fig. 4(b) and Fig. 4(c) illustrate the gradient results of Phantom D across different methods. The solid line in the strip charts of Fig. 4(b) indicates that the median APT intensity in each row changes with the column number, while the bandwidth represents the upper and lower quartiles (analogously with NOE evaluation in Fig. 4(c)). The dashed line is the ground truth gradient. LINR effectively balances the preservation of constant intensity and sensitivity

to intensity variations in both the APT and NOE maps. In contrast, methods like MPF and PLOF fail to maintain stability in constant regions, and NLM struggles with detecting subtle gradient changes.

To further evaluate the robustness of each method to varying noise levels, we added Gaussian noise to the phantoms in increments of 0.01, ranging from 0.01 to 0.1 standard deviation, and compared the Peak Signal-to-Noise Ratio (PSNR) in phantoms containing molecular signals, which is defined as

$$PSNR = 10 \log_{10} \left(\frac{MAX_I^2}{MSE} \right),$$

where MAX_I is the maximum signal intensity and MSE is the mean squared error between the ground truth and reconstructed maps. LINR consistently maintained the highest PSNR and kept it above 35 dB even at the most severe noise levels.

C. Brain Tumor

CEST contrasts can reveal significant pathological features in brain tumors. Specifically, the tumor region appears hyperintense on the APT map compared to the contralateral normal-appearance white matter (CNAWM), while it shows the opposite effect on the NOE and GuanCEST maps [10], [15]. These characteristics effectively validate whether a CEST analysis method accurately extracts the CEST effect.

Validation of CEST maps is visualized in Fig. 5. The boxplots imply that both methods detect tumors in terms of three molecular levels accurately and with strong confidence. Unlike MPF, which was carefully set for this subject, LINR provides CEST maps without the requirement of a subject-specific setup. Nonetheless, LINR is still capable of giving CEST contrasts that match tumor shape and pathology with high sensitivity, referring to the T2w image, while the CEST contrast by MPF shows weak consistency with the tumor shape, especially in APT and GuanCEST maps. Furthermore, CEST maps generated by LINR reveal clear details of other structures in the brain. Notably, the green arrow in the T2w image points to a group of low-brightness cells within the hyperintense tumor area, suggesting they are normal-appearance cells. From the maps, it is evident that LINR accurately identified the CEST contrasts of this group of cells, showing intensity similar to normal cells and distinctly different from the tumor. In contrast, the traditional MPF did not detect a clear difference in the CEST effect for this area compared to its surroundings, demonstrating LINR's exceptional sensitivity.

Since Lorentzian-based CEST analysis focuses on unveiling the relative contrast of tissues with respect to exchangeable pools rather than their absolute values, maps generated by different methods may exhibit mean differences. We further employed the Fourier transform to convert the maps from both methods into the frequency domain for correlation analysis, as displayed in Fig. 6. As the logarithm is applied to each frequency matrix, whose patterns can be seen more significantly, MPF and LINR share a strong similarity in the frequency domain. Given that the intensity distribution of MPF and LINR are perfectly overlapped, as suggested

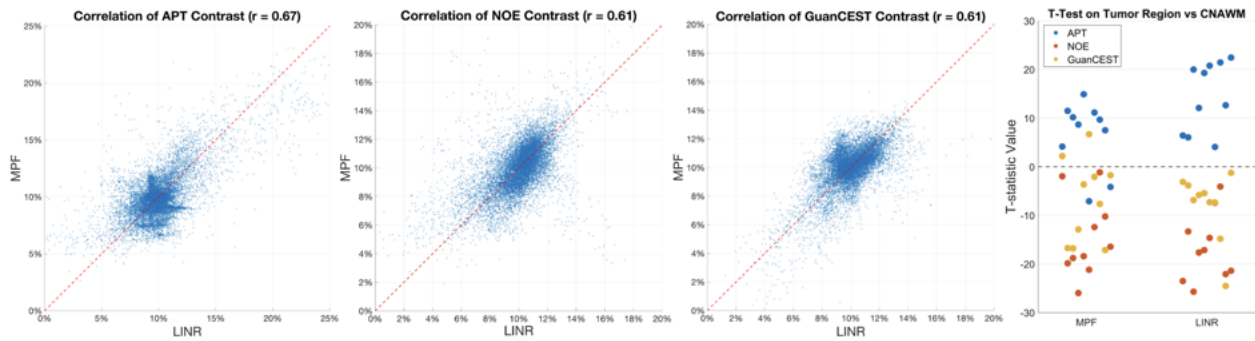


Fig. 7. Correlation evaluation and pathology t-test on the overall tumor dataset. The three scatter plots on the left show the frequency domain correlation of CEST contrasts given by two methods across all 10 samples. The correlation coefficients are indicated in the subtitles, and the ideal correlation is in red dashed lines. The scatter plot on the far right compares the CEST contrasts from both methods between the tumor region and the CNAWM, based on hypothesis testing guided by pathology. A positive T-statistic indicates higher intensity in the tumor region, while a negative value suggests the opposite.

by the histograms below, CEST maps generated by the two methods are strongly consistent. However, the GuanCEST signal, positioned between the water signal and APT signal, often poses challenges for MPF optimization in accurately capturing GuanCEST contrast. As shown in Fig. 6(c), MPF’s GuanCEST frequency domain distribution lacks a significant pattern, whereas LINR demonstrates similar patterns in the high-frequency range across various contrasts. This suggests that MPF performs poorly in capturing texture details about tissues.

What’s more, we take a step further to conduct correlation and pathology studies across all mice within the tumor dataset. The correlation analysis of APT, NOE, and GuanCEST contrasts are shown in Fig. 7, and correlation coefficients are indicated in the title. Since CEST contrasts obtained by two algorithms could exhibit different absolute values in the image domain and MPF is not as sensitive as LINR, the maps given by these methods could not be perfectly correlated. Nonetheless, across three types of contrast in 10 mice, LINR and the object-specific adjusted MPF demonstrated a high correlation, indicating LINR’s robust stability, accuracy, and sensitivity in capturing the CEST effect. By referring to the far right T-test result on CEST contrasts in Fig. 7, all ten APT contrasts provided by LINR indeed reveal hyperintense tumor regions compared to CNAWM, given that T-statistics are positive, while negative T-statistics in NOE and GuanCEST imply hypointense tumor regions. Leveraging the universal approximation capability of neural networks, LINR consistently produced CEST contrast maps in line with tumor pathology for all subjects, whereas MPF failed to accurately fit two cases in the APT and GuanCEST maps.

D. Alzheimer’s Disease

Numerous studies have shown that CEST imaging can reveal molecular-level pathological features of AD [17]–[19]. Specifically, protein aggregation in AD mice brains increases macromolecular rigidity, impairing proton exchange dynamics critical for CEST detection [18], [19], [45], while AD-associated neuroinflammation induces tissue acidosis, which suppresses the chemical exchange rate, as validated in prior CEST-MRI studies [17]. In general, individuals with AD

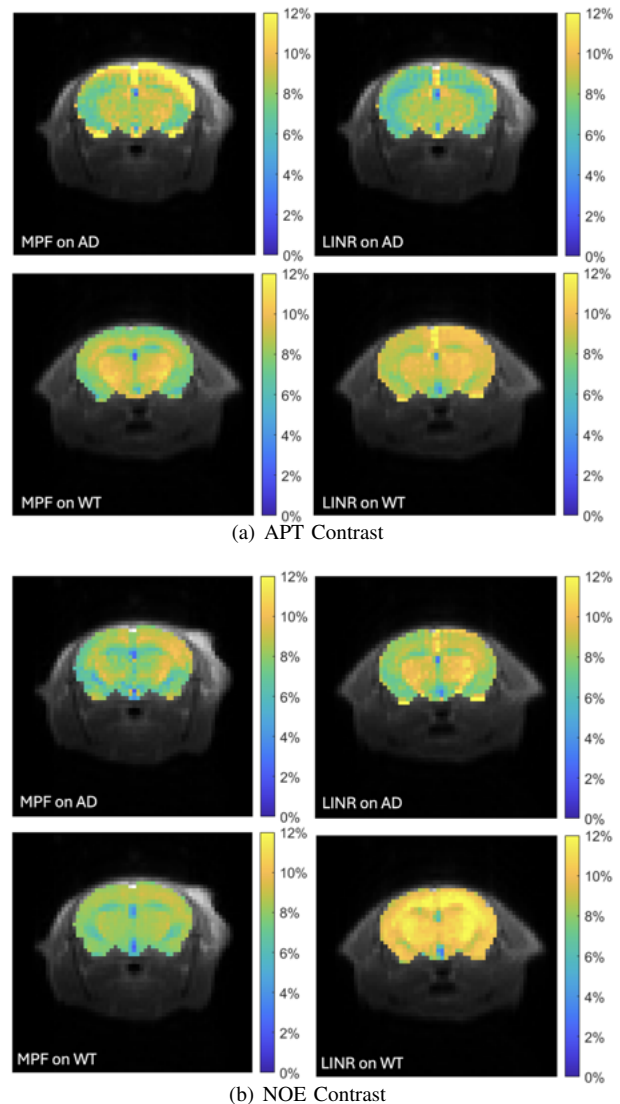


Fig. 8. CEST analysis on AD and WT mouse. Color CEST contrasts of the brain are overlaid on the averaged M0 image, where mouse types and analysis methods are specified at the corner of each subfigure.

exhibit overall lower APT and NOE effects in the brain compared to healthy wild-type (WT) subjects.

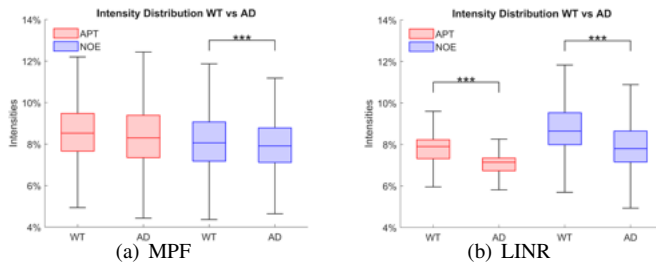


Fig. 9. The box plots comparing the intensity distributions of APT and NOE maps in the brain regions of AD and WT subjects using two methods: MPF and LINR. The top plot (a) uses the MPF method, while the bottom plot (b) uses LINR. *** p -value < 0.001 .

Fig. 8 demonstrates the APT and NOE contrasts obtained through MPF and LINR methods for an AD mouse brain and a WT mouse brain. Comparing the APT contrast from MPF, the overall intensity in the brain of the AD individual is slightly lower than that of the WT. However, the NOE contrast does not exhibit this pathological difference. In contrast, the LINR method accurately identifies the pathological distinctions in CEST contrast between AD and WT.

In addition, we tested the robustness of the method across the entire AD dataset of 25 individuals, comparing the CEST effect intensity in the brains of 15 AD mice and 10 WT mice, as shown in Fig. 9. It reveals that the LINR method provides clearer differentiation between groups than the MPF method. With LINR, there is a significant and distinct separation in both APT and NOE intensities, indicated by a higher median as well as a greater overall distribution. These differences are statistically significant, with a p -value < 0.001 , illustrating LINR's superior sensitivity and robustness in capturing pathological features related to CEST effects, whereas MPF shows less distinct separation, particularly for APT contrasts.

V. CONCLUSION

This paper proposed a self-supervised framework, the Lorentzian-model Informed Neural Representation (LINR), for effective and high-quality CEST mapping. This algorithm incorporates the physical model priors of the CEST data with the ability of the neural network to represent the Lorentzian parameter spaces. An additional denoising module enhances mapping accuracy. Compared to existing methods, LINR eliminates the necessity for external training datasets and empirical estimates of molecule-related parameters, demonstrating exceptional adaptability in practical implementations. By constructing a Lorentzian Neural Tangent Kernel (LNTK) and examining its properties, we present a theorem that guarantees the convergence of the optimization process in MappingNet.

Quantitative evaluations on simulated phantom data have shown superior mapping precision of LINR and its robustness against noise. In addition, LINR was applied to brain tumors and Alzheimer's disease datasets to demonstrate in-vivo applications. The resulting contrasts validate its mapping abilities and the sensitivity of multi-molecular contrasts compared to traditional algorithms. Thus, LINR promises a significant advancement in the field of molecular-level disease research with CEST MRI.

REFERENCES

- [1] C. Chen *et al.*, "Implicit regression in subspace for high-sensitivity cest imaging," in *2024 IEEE International Symposium on Biomedical Imaging (ISBI)*. IEEE, 2024, pp. 1–5.
- [2] J. Zhou *et al.*, "Differentiation between glioma and radiation necrosis using molecular magnetic resonance imaging of endogenous proteins and peptides," *Nature Medicine*, vol. 17, no. 1, pp. 130–134, 2011.
- [3] M. Haris *et al.*, "A technique for in vivo mapping of myocardial creatine kinase metabolism," *Nature Medicine*, vol. 20, no. 2, pp. 209–214, 2014.
- [4] L. Chen *et al.*, "In vivo imaging of phosphocreatine with artificial neural networks," *Nature Communications*, vol. 11, no. 1, p. 1072, 2020.
- [5] P. Jabejdar Maralani *et al.*, "Chemical exchange saturation transfer mri: what neuro-oncology clinicians need to know," *Technology in Cancer Research & Treatment*, vol. 22, p. 15330338231208613, 2023.
- [6] L. Consolino *et al.*, "Non-invasive investigation of tumor metabolism and acidosis by mri-cest imaging," *Frontiers in Oncology*, vol. 10, p. 161, 2020.
- [7] S. Goerke *et al.*, "Relaxation-compensated apt and rnoe cest-mri of human brain tumors at 3 t," *Magnetic Resonance in Medicine*, vol. 82, no. 2, pp. 622–632, 2019.
- [8] Y. Zhao *et al.*, "Assignment of molecular origins of noe signal at 3.5 ppm in the brain," *Magnetic Resonance in Medicine*, vol. 90, no. 2, pp. 673–685, 2023.
- [9] Z. Zu *et al.*, "Relayed nuclear overhauser enhancement sensitivity to membrane cho phospholipids," *Magnetic Resonance in Medicine*, vol. 84, no. 4, pp. 1961–1976, 2020.
- [10] K. Cai *et al.*, "Cest signal at 2 ppm (cest@ 2ppm) from z-spectral fitting correlates with creatine distribution in brain tumor," *NMR in Biomedicine*, vol. 28, no. 1, pp. 1–8, 2015.
- [11] J. Xu *et al.*, "Chemical exchange saturation transfer imaging of creatine, phosphocreatine, and protein arginine residue in tissues," *NMR in Biomedicine*, vol. 36, no. 6, p. e4671, 2023.
- [12] A. A. Sehgal *et al.*, "Cest mri of 3-o-methyl-d-glucose uptake and accumulation in brain tumors," *Magnetic Resonance in Medicine*, vol. 81, no. 3, pp. 1993–2000, 2019.
- [13] K. Cai *et al.*, "Magnetic resonance imaging of glutamate," *Nature Medicine*, vol. 18, no. 2, pp. 302–306, 2012.
- [14] J. Cui and Z. Zu, "Towards the molecular origin of glutamate cest (glucest) imaging in rat brain," *Magnetic Resonance in Medicine*, vol. 83, no. 4, pp. 1405–1417, 2020.
- [15] J. Huang *et al.*, "Molecular imaging of brain tumors and drug delivery using cest mri: promises and challenges," *Pharmaceutics*, vol. 14, no. 2, p. 451, 2022.
- [16] A. Tietze *et al.*, "Assessment of ischemic penumbra in patients with hyperacute stroke using amide proton transfer (apt) chemical exchange saturation transfer (cest) mri," *NMR in Biomedicine*, vol. 27, no. 2, pp. 163–174, 2014.
- [17] L. Chen *et al.*, "Early detection of alzheimer's disease using creatine chemical exchange saturation transfer magnetic resonance imaging," *Neuroimage*, vol. 236, p. 118071, 2021.
- [18] J. Huang *et al.*, "Deep neural network based cest and arex processing: Application in imaging a model of alzheimer's disease at 3 t," *Magnetic Resonance in Medicine*, vol. 87, no. 3, pp. 1529–1545, 2022.
- [19] L. Chen *et al.*, "Protein aggregation linked to alzheimer's disease revealed by saturation transfer mri," *Neuroimage*, vol. 188, pp. 380–390, 2019.
- [20] I. Yuwen Zhou *et al.*, "Direct saturation-corrected chemical exchange saturation transfer mri of glioma: Simplified decoupling of amide proton transfer and nuclear overhauser effect contrasts," *Magnetic Resonance in Medicine*, vol. 78, no. 6, pp. 2307–2314, 2017.
- [21] Y. Wu *et al.*, "Fast and equilibrium cest imaging of brain tumor patients at 3t," *Neuroimage: Clinical*, vol. 33, p. 102890, 2022.
- [22] L. Chen *et al.*, "Creatine and phosphocreatine mapping of mouse skeletal muscle by a polynomial and lorentzian line-shape fitting cest method," *Magnetic Resonance in Medicine*, vol. 81, no. 1, pp. 69–78, 2019.
- [23] F. Glang *et al.*, "Deepcest 3t: Robust mri parameter determination and uncertainty quantification with neural networks—application to cest imaging of the human brain at 3t," *Magnetic Resonance in Medicine*, vol. 84, no. 1, pp. 450–466, 2020.
- [24] J. R. Rajput *et al.*, "Physics-informed conditional autoencoder approach for robust metabolic cest mri at 7t," in *International Conference on Medical Image Computing and Computer-Assisted Intervention*. Springer, 2023, pp. 449–458.
- [25] M. Singh *et al.*, "Bloch simulator-driven deep recurrent neural network for magnetization transfer contrast mr fingerprinting and cest imaging," *Magnetic Resonance in Medicine*, vol. 90, no. 4, pp. 1518–1536, 2023.

- [26] Z. Yang *et al.*, "Attention-based multioffset deep learning reconstruction of chemical exchange saturation transfer (amo-cest) mri," *IEEE Journal of Biomedical and Health Informatics*, 2024.
- [27] L. Chen *et al.*, "High-sensitivity cest mapping using a spatiotemporal correlation-enhanced method," *Magnetic Resonance in Medicine*, vol. 84, no. 6, pp. 3342–3350, 2020.
- [28] F. Romdhane *et al.*, "Evaluation of a similarity anisotropic diffusion denoising approach for improving in vivo cest-mri tumor ph imaging," *Magnetic Resonance in Medicine*, vol. 85, no. 6, pp. 3479–3496, 2021.
- [29] H. Chen *et al.*, "Learned spatiotemporal correlation priors for cest image denoising using incorporated global-spectral convolution neural network," *Magnetic Resonance in Medicine*, 2023.
- [30] Y. Kurmi *et al.*, "Enhancing snr in cest imaging: A deep learning approach with a denoising convolutional autoencoder," *Magnetic Resonance in Medicine*, vol. 92, no. 6, pp. 2404–2419, 2024.
- [31] M. Zaiß *et al.*, "Quantitative separation of cest effect from magnetization transfer and spillover effects by lorentzian-line-fit analysis of z-spectra," *Journal of Magnetic Resonance*, vol. 211, no. 2, pp. 149–155, 2011.
- [32] M. Huemer *et al.*, "Improved quantification in cest-mri by joint spatial total generalized variation," *Magnetic Resonance in Medicine*, 2024.
- [33] K. Wang *et al.*, "Guanidinium and amide cest mapping of human brain by high spectral resolution cest at 3 t," *Magnetic Resonance in Medicine*, vol. 89, no. 1, pp. 177–191, 2023.
- [34] K. Wang *et al.*, "Whole-cerebrum guanidino and amide cest mapping at 3 t by a 3d stack-of-spirals gradient echo acquisition," *Magnetic Resonance in Medicine*, vol. 92, no. 4, pp. 1456–1470, 2024.
- [35] V. Sitzmann *et al.*, "Implicit neural representations with periodic activation functions," *Advances in Neural Information Processing Systems*, vol. 33, pp. 7462–7473, 2020.
- [36] V. Saragadam *et al.*, "Wire: Wavelet implicit neural representations," in *Proceedings of the IEEE/CVF Conference on Computer Vision and Pattern Recognition (CVPR)*, June 2023, pp. 18 507–18 516.
- [37] B. Mildenhall *et al.*, "Nerf: Representing scenes as neural radiance fields for view synthesis," *Communications of the ACM*, vol. 65, no. 1, pp. 99–106, 2021.
- [38] B. Liu *et al.*, "Scan-specific unsupervised highly accelerated non-cartesian cest imaging using implicit neural representation and explicit sparse prior," *IEEE Transactions on Biomedical Engineering*, 2024.
- [39] T. Blu and F. Luisier, "The sure-let approach to image denoising," *IEEE Transactions on Image Processing*, vol. 16, no. 11, pp. 2778–2786, 2007.
- [40] J. Li *et al.*, "Subspace modeling enabled high-sensitivity x-ray chemical imaging," in *ICASSP 2023 - 2023 IEEE International Conference on Acoustics, Speech and Signal Processing (ICASSP)*, 2023, pp. 1–5.
- [41] X.-Y. Zhang *et al.*, "Assignment of the molecular origins of cest signals at 2 ppm in rat brain," *Magnetic Resonance in Medicine*, vol. 78, no. 3, pp. 881–887, 2017.
- [42] L. Chen *et al.*, "Investigation of the contribution of total creatine to the cest z-spectrum of brain using a knockout mouse model," *NMR in Biomedicine*, vol. 30, no. 12, p. e3834, 2017.
- [43] A. Jacot *et al.*, "Neural tangent kernel: Convergence and generalization in neural networks," *Advances in Neural Information Processing Systems*, vol. 31, 2018.
- [44] S.-W. Park *et al.*, "Preclinical application of cest mri to detect early and regional tumor response to local brain tumor treatment," *Pharmaceutics*, vol. 16, no. 1, p. 101, 2024.
- [45] J. A. Wells *et al.*, "In vivo imaging of tau pathology using multi-parametric quantitative mri," *Neuroimage*, vol. 111, pp. 369–378, 2015.